iScience

CellPress
OPEN ACCESS

Article

Cation-π induced surface cleavage of organic pollutants with $^{\bullet}OH$ formation from H_2O for water treatment

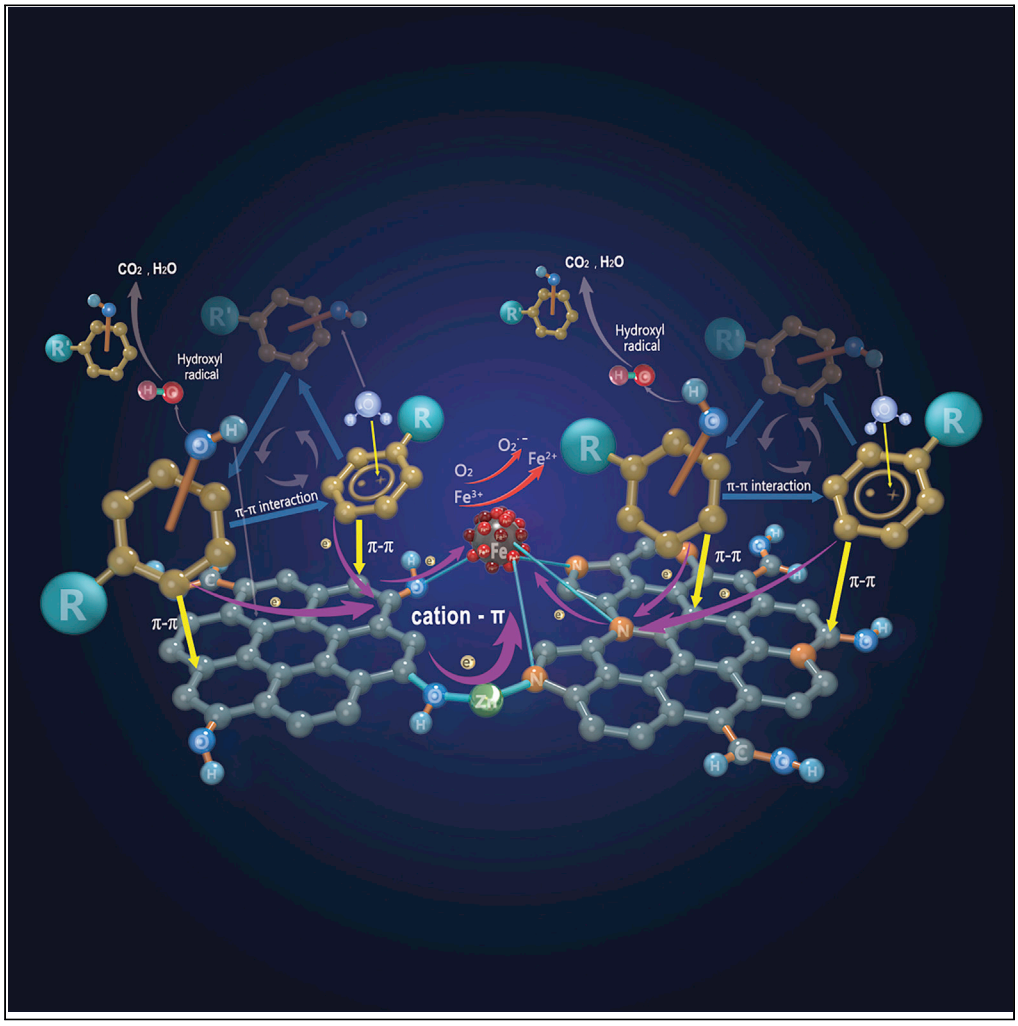

Yumeng Wang, Lai Lyu, Di Wang, ..., John C. Crittenden, Lili Zhang, Chun Hu

huchun@gzhu.edu.cn

Highlights

A strong Fe-π interaction occurs on the surface of Fe^0-Fe_yC_z/Fe_x-GZIF-8-rGO

The electrostatic force causes the surface potential energy ~310.97 to 663.96 kJ/mol

The refractory organics undergo surface cleavage with H_2O to $^{\bullet}OH$ on the catalyst

The pollutants are removed in the air-saturated suspension without additional energy

Wang et al., iScience 24, 102874
August 20, 2021
https://doi.org/10.1016/j.isci.2021.102874

iScience

CellPress
OPEN ACCESS

Article

Cation-π induced surface cleavage of organic pollutants with ˙OH formation from H_2O for water treatment

Yumeng Wang,[1,5] Lai Lyu,[1,5] Di Wang,[1] Han-Qing Yu,[2] Tong Li,[1] Yaowen Gao,[1] Fan Li,[1] John C. Crittenden,[3] Lili Zhang,[4] and Chun Hu[1,6,*]

SUMMARY

High energy consumption is impedimental for eliminating refractory organic pollutants in water by applying advanced oxidation processes (AOPs). Herein, we develop a novel process for destructing these organics in chemical conjuncted Fe^0-Fe_yC_z/Fe_x, graphited ZIF-8, and rGO air-saturated aqueous suspension without additional energy. In this process, a strong Fe-π interaction occurs on the composite surface, causing the surface potential energy ~310.97 to 663.96 kJ/mol. The electrons for the adsorbed group of pollutants are found to delocalize to around the iron species and could be trapped by O_2 in aqueous suspension, producing ˙OH, H, and adsorbed organic cation radicals, which are hydrolyzed or hydrogenated to intermediate. The target pollutants undergo surface cleavage and convert H_2O to ˙OH, consuming chemical adsorption energy (~2.852–9.793 kJ/mol), much lower than that of AOPs. Our findings provide a novel technology for water purification and bring new insights into pollutant oxidation chemistry.

INTRODUCTION

Thousands of industrial chemical compounds that are present in aquatic systems pose severe health problems worldwide (Bullock, 2003). Many of them may have considerable toxicological consequences at environmental concentrations, particularly when they are present as components of complex mixtures (Schwarzenbach et al., 2006). Moreover, these substances are the necessities of human society development, such as pharmaceuticals and detergents. Accordingly, it is important to develop and apply cost-effective water purification technologies.

To date, advanced oxidation processes (AOPs) have been recognized as the most effective method for converting organics into carbon dioxide, water, and other organic acids by continuous attacking of hydroxyl radicals (˙OH). ˙OH can be generated by a combination of oxidants (e.g., O_3, H_2O_2), irradiation, and catalysts (Adewuyi, 2005; Lee et al., 2020), which results in very high energy consumption. As a result, the AOPs are rarely applied to eliminate organic pollutants at a large scale. Most of the organic pollutants possess very high chemical energy, but these reactant energies have not been effectively utilized for water purification (Li et al., 2015b; Abednatanzi et al., 2020). Cation-π interactions are electrostatic attractions between cations and electron-rich π orbitals (Gebbie et al., 2017). A strong cation-π binding occurs when cations interact with delocalized π orbitals perpendicular to the plane of aromatic rings (Dougherty, 1996), exceeding the strength of hydrogen bonds, and possibly even charge-charge interactions, in aqueous solutions (Ma and Dougherty, 1997; Deakyne and Meot-Ner, 1985). Since Dougherty came up with the concept of cation-π interaction in 1990, cation-π interactions have been widely studied in structural biology, supramolecular chemistries, neurobiology, etc. (Yamada, 2018; Salonen, et al., 2011). In addition, charge transfer has been observed in transition metal ion-π interactions from the complex of transition metal ions with phenolic organic pollutants (Lagutschenkov et al., 2010). Our recent studies (Lyu et al., 2017, 2018a, 2018b; Jiang et al., 2018) indicate that, in a dual-reaction center Fenton-like system, by cation-π interaction, the energy of some organic pollutants and their intermediates as electron donors can be used to reduce H_2O_2 in the electron-rich area. Also, pollutants are degraded by losing electrons at the electron-poor area rather than being attacked by ˙OH. In this situation, about 90% H_2O_2 is utilized and a high degree of organic pollutants are oxidized. With an increase in the cation-π interaction, the

[1]Key Laboratory for Water Quality and Conservation of the Pearl River Delta, Ministry of Education, Institute of Environmental Research at Greater Bay, Guangzhou University, Guangzhou 510006, China

[2]CAS Key Laboratory of Urban Pollutant Conversion, Department of Applied Chemistry, University of Science and Technology of China, Hefei 230026, China

[3]Brook Byers Institute for Sustainable Systems, School of Civil and Environmental Engineering, Georgia Institute of Technology, Atlanta, GA 30332, USA

[4]Research Center for Eco-Environmental Sciences, Chinese Academy of Sciences, Beijing 100085, China

[5]These authors contributed equally

[6]Lead contact

*Correspondence: huchun@gzhu.edu.cn

https://doi.org/10.1016/j.isci.2021.102874

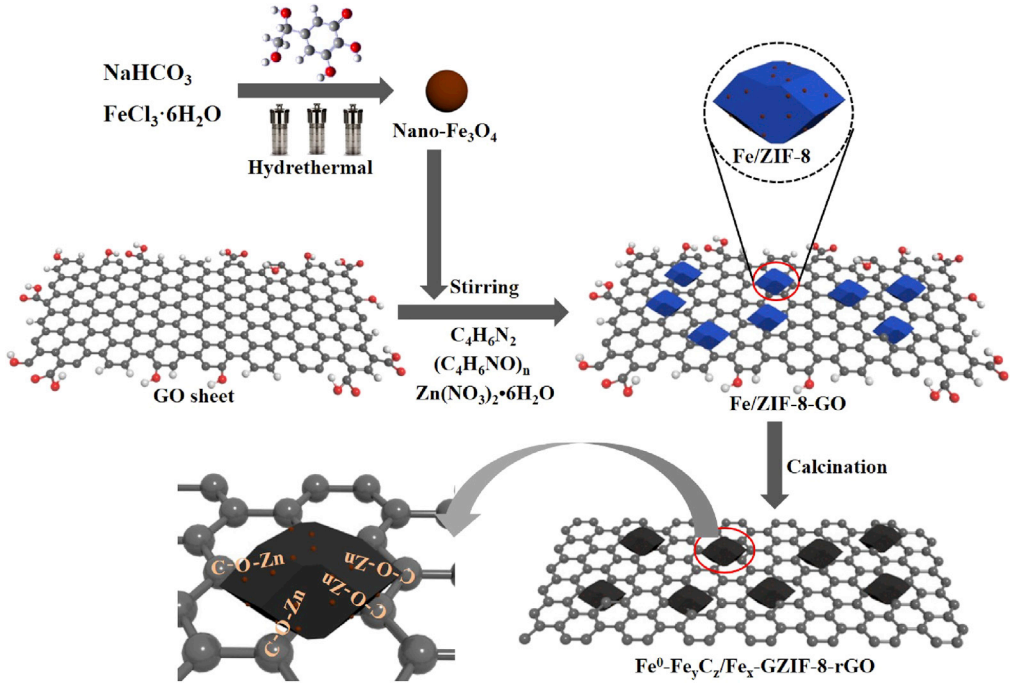

Figure 1. Preparation of Fe^0-Fe_yC_z/Fe_x-GZIF-8-rGO

Schematic illustration of the preparation of Fe^0-Fe_yC_z/Fe_x-GZIF-8-rGO.

consumption of H_2O_2 was greatly decreased in $CoMoS_2$ nanosphere-embedded rGO nanosheets (Han et al., 2019) owing to the reduction of O_2 to H_2O_2 using energy of the pollutants. Therefore, the strong cation-π interaction provides a feasibility of utilizing the energy of the organic pollutants.

Reduced graphene (rGO) is capable of π-π interactions with aromatic molecules (Georgakilas et al., 2012), adsorbing most of organic pollutants by π-π stacking and hydrogen bonding (Teixido et al., 2011; Algara-Siller et al., 2015). Thus, electrons of organics are transferred to the surfaces of metal oxides that are complexed by rGO via the transition metal ion-π interaction without additional energy.

Herein, a composite catalyst Fe^0-Fe_yC_z/Fe_x-GZIF-8-rGO is synthesized as described in Figure 1. Various persistent organic pollutants (Table S1) including pharmaceuticals (ibuprofen, ciprofloxacin, phenytoin, and diphenhydramine), pesticides (2-chlorophenol, 2,4-dichlorophenoxyaceticacid), and endocrine disrupting chemicals (bisphenol A) were selected to evaluate the performance of our catalytic system because of their presence in water and adverse ecotoxicological effects. The degradation and mineralization performances of the target pollutants were examined in the air-saturated or N_2-saturated water containing Fe^{3+} and an aqueous suspension of our catalyst. The surface reaction mechanism induced by strong cation-π electrostatic force was proposed for the cleavage of adsorbed pollutants and $^{\bullet}OH$ production from H_2O based on both experimental results and density-functional theory (DFT) calculations.

RESULTS AND DISCUSSION

Characteristics of Fe^0-Fe_yC_z/Fe_x-GZIF-8-rGO

In the X-ray diffraction (XRD) pattern of Fe^0-Fe_yC_z/Fe_x-GZIF-8-rGO (Figure 2A), three diffraction peaks at 2θ = 42.9°, 43.5°, and 49.2° were ascribed to Fe_3C; a peak at 44.6° was ascribed to Fe^0; and peaks at 50.6°, 57.4°, and 74.2° were ascribed to Fe_3O_4. The diffraction peaks at 2θ = 10.4° and 26.3° were assigned to rGO (Wu et al., 2019; Moon et al., 2010; Meng et al., 2013). The XRD peak of the ZIF-8 sample, which was prepared by the same procedure, appeared at 24.9° in the inset of Figure 2A, indicating that ZIF-8 became a graphited carbon skeleton (GZIF-8) after the calcination at 700°C (Gu et al., 2019). Therefore, GZIF-8 also contributed to the diffraction peak at 26.3° in Fe^0-Fe_yC_z/Fe_x-GZIF-8-rGO. Based on the hyperfine parameters (Table S2), the fitting curves from the room temperature ^{57}Fe Mössbauer spectra of Fe^0-Fe_yC_z/Fe_x-GZIF-8-rGO (Figure 2B) exhibited three sextets for Fe_xC_y, Fe_3C and α-Fe; a doublet for $Fe_{2+x}N$; and a singlet for α-Fe and γ-Fe (Zitolo

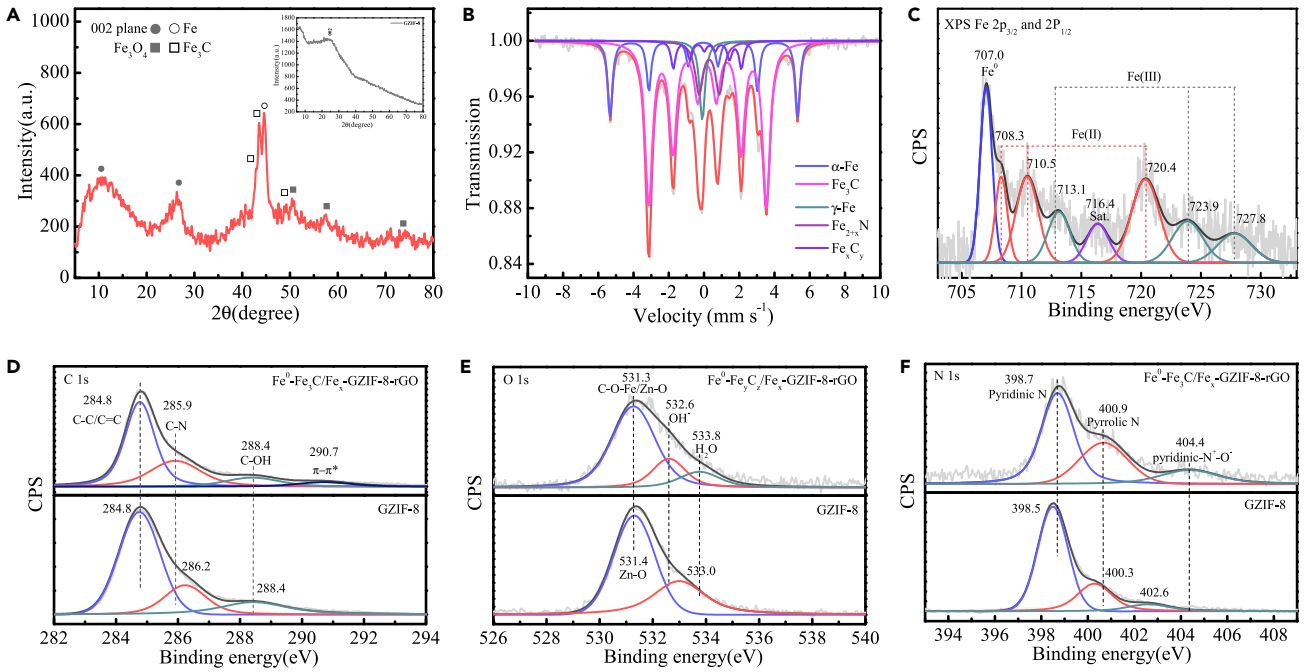

Figure 2. Structural characterization of Fe^0-Fe_yC_z/Fe_x-GZIF-8-rGO

(A) XRD pattern of Fe^0-Fe_yC_z/Fe_x-GZIF-8-rGO (Inset: XRD pattern of GZIF-8).

(B) Room temperature ^{57}Fe Mössbauer spectrum of Fe^0-Fe_yC_z/Fe_x-GZIF-8-rGO.

(C–F) (C) Fe 2p XPS, (D) C 1s XPS, (E) O 1s XPS, and (F) N 1s XPS spectra of Fe^0-Fe_yC_z/Fe_x-GZIF-8-rGO and GZIF-8.

et al., 2015; Wang et al., 2018; Liang et al., 2019). No Fe_3O_4 phase was detected, indicating its low content in the composite. The existence of $Fe_{2+x}N$ revealed that relative amounts of Fe(II) and Fe(III) were coordinated to the N atoms, and most of the Fe atoms were Fe^0 existing as α-Fe, γ-Fe, Fe_xC_y, and Fe_3C. These results indicated that the catalyst predominantly consisted of three phases: Fe^0-Fe_yC_z/Fe_x, GZIF-8, and rGO.

In X-ray photoelectron spectroscopy (XPS) of Fe^0-Fe_yC_z/Fe_x-GZIF-8-rGO, the Fe 2p XPS spectra (Figure 2C) showed peaks at 708.3, 710.5, and 720.4 eV and were assigned to Fe(II), whereas those at 713.1, 723.9, and 727.8 eV were assigned to Fe(III), along with a shakeup satellite peak at 716.4 eV (Tang and Wang, 2018; Jin et al., 2017). In addition, a strong peak for Fe^0 appeared at 707.0 eV (Li et al., 2015a, 2015b). In the C 1s XPS spectra (Figure 2D), the peak at 284.8 eV was assigned to C=C of the aromatic rings in GZIF-8 and rGO, the peak at 286.2 eV was ascribed to C–N of GZIF-8, and the peak at 288.4 eV was ascribed to C–OH of rGO (Zhang et al., 2011). In the O 1s XPS (Figure 2E), the two peaks at 532.6 and 533.8 eV were attributed to the surface OH^- and H_2O. The peak at 531.3 eV was attributed to the lattice oxygen of C–O–Fe or C–O–Zn. The peak at 530.1 eV is typically ascribed to Fe–O–Fe in Fe_3O_4 but it was not present, indicating that an insignificant amount of Fe_3O_4 existed on the surface of the composite, confirming the ^{57}Fe Mössbauer spectra.

The binding energies of Zn $2p_{3/2}$ (1,021.8 eV) and Zn $2p_{1/2}$ (1,044.9 eV) for Fe^0-Fe_yC_z/Fe_x-GZIF-8-rGO were higher than those for GZIF-8 (1,021.6 and 1,044.8 eV) (Figure S1A), whereas the binding energies (531.5 and 288.4 eV) of both O 1s and C 1s for C–O in Fe^0-Fe_yC_z/Fe_x-GZIF-8-rGO were lower than those for rGO (532.6 and 288.5 eV) (Figures S1B and S1C). These results indicated that both N–Zn–O–C and Fe–O–C bonds formed between the O atoms of the phenolic groups in rGO and the Zn atom in GZIF-8 or Fe(III) in Fe^0-Fe_yC_z/Fe_x (Li et al., 2016) (Figure S1D). The N 1s XPS spectra of Fe^0-Fe_yC_z/Fe_x-GZIF-8-rGO (Figure 2F) show the peaks corresponding to pyridinic N (398.7eV), pyrrolic N (400.9 eV), and pyridinic N^+–O^- (404.4 eV) of the GZIF-8 carbon skeleton (Liu et al., 2009), which are higher than those of the pure GZIF-8 sample, indicating the formation of the Fe-N complexes.

In Fe K-edge extended X-ray absorption fine structure (EXAFS) spectroscopy (Figure 3A), a distinct Fe–Fe coordination shell at 2.08 Å was observed in Fe^0-Fe_yC_z/Fe_x-GZIF-8-rGO, which is similar to the Fe–Fe shell of Fe foil, confirming the existence of the Fe^0 species. And the slight deviation in this shell from the Fe foil

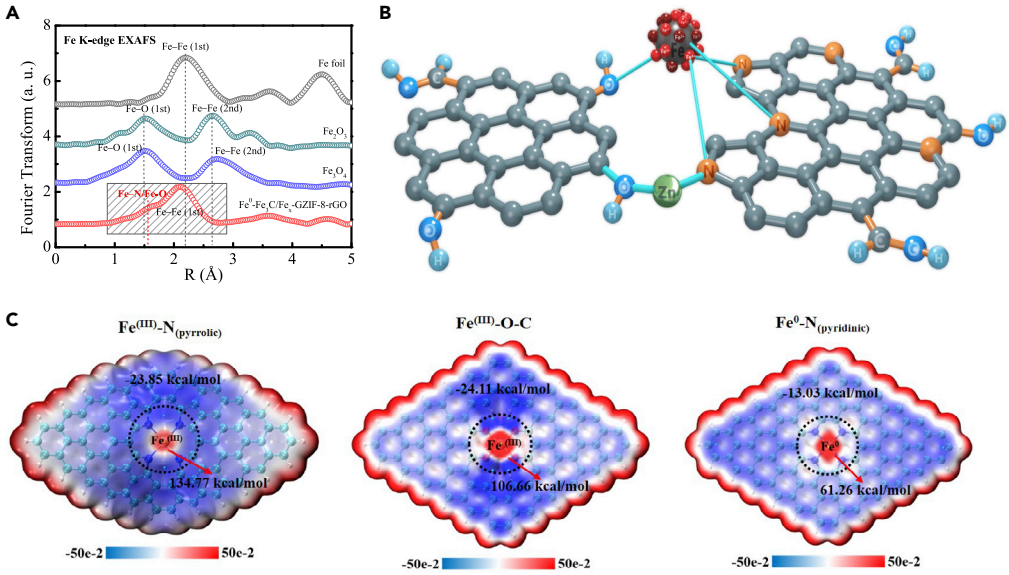

Figure 3. Surface structure and uneven electron distribution of Fe^0-Fe_yC_z/Fe_x-GZIF-8-rGO

(A) Fourier transforms of the k^3-weighted EXAFS oscillations obtained at the Fe K-edge of the various samples.

(B) Configuration of Fe^0-Fe_yC_z/Fe_x-GZIF-8-rGO.

(C) ESP distribution for different structural model fragments of Fe^0-Fe_yC_z/Fe_x-GZIF-8-rGO.

indicated that the coordination environment of Fe in Fe^0-Fe_yC_z/Fe_x-GZIF-8-rGO was influenced by the coordinated elements, which was also confirmed by the appearance of the protruding Fe–X coordination shells at 1–2 Å (no phase correction) in Fe^0-Fe_yC_z/Fe_x-GZIF-8-rGO. From advanced fitting of the EXAFS spectra (Figure S2), both Fe–$N_{(3.3)}$ and Fe–$O_{(2)}$ were detected in Fe^0-Fe_yC_z/Fe_x-GZIF-8-rGO (Table S3). The short bond distance (R = 1.3 Å) of Fe–N indicates that N was in the first coordination layer of Fe, confirming the formation of Fe–N bonds (Chen et al., 2018). However, the bond distance (R = 2.44 Å) of the Fe–O shell in Fe^0-Fe_yC_z/Fe_x-GZIF-8-rGO was much larger than that (R = 1.97 Å) of the pure Fe_3O_4 sample (van Genuchten et al., 2018), indicating that the Fe–O bond on the Fe^0-Fe_yC_z/Fe_x-GZIF-8-rGO surface was mainly from the coordination of Fe(II)/Fe(III) with the hydroxyl group in the aromatic ring of rGO, rather than from the lattice O of Fe_3O_4. These results also indicate that Fe(II)/Fe(III) on the surface were predominantly complexed by pyridinic N, the pyrrolic N group of GZIF-8, or the hydroxyl group of rGO, forming coordination bonds among three phases.

In the Raman spectra (Figure S3), the D band peaks at ~1,333 cm^{-1} and the G band peaks at ~1,592 cm^{-1} were observed in all the samples, which originated from the defects/disordered carbon and the ordered structure of the sp^2 carbon atoms, respectively (Yang et al., 2020). Fe^0-Fe_yC_z/Fe_x-GZIF-8-rGO exhibited a higher ratio of I_D/I_G (1.06) than GZIF-8-rGO (0.99), GZIF-8 (0.99), and GO (0.97), indicating that more defects were produced in Fe^0-Fe_yC_z/Fe_x-GZIF-8-rGO (Luo et al., 2013). In addition, GZIF-8 exhibited a peak analogous to that of pure GO at 2,646 cm^{-1}, which was assigned to the 2D band of GO (Wang et al., 2014). This indicated the formation of a graphene-like structure in GZIF-8 and confirmed the XRD results. Based on the above results, the structure of Fe^0-Fe_yC_z/Fe_x-GZIF-8-rGO was proposed as shown in Figure 3B. Three chemical coordination bonds were formed in the interface of different phases, including Fe–O–C between Fe^0-Fe_yC_z/Fe_x and rGO, Fe–N between Fe^0-Fe_yC_z/Fe_x and GZIF-8, and C–O–Zn–N between GZIF-8 and rGO. Moreover, these coordination bonds were all connected to the aromatic rings of rGO and GZIF-8 by phenolic group, pyridinic N, or pyrrolic N. Therefore, a particularly strong cation (Fe or Zn)-π interaction occurred with the delocalized π orbitals perpendicular to the plane of the aromatic rings via an electrostatic force. Three kinds of optimal structural model fragments were constructed involving $Fe^{(III)}$–$N_{(pyrrolic)}$, $Fe^{(III)}$–O–C, and Fe^0–$N_{(pyridinic)}$ of Fe^0-Fe_yC_z/Fe_x-GZIF-8-rGO. The electrostatic surface potential (ESP) distribution was calculated employing DFT methods. For all the model segments, the highest electrostatic potential (61.26–134.77 kcal/mol) (red) appeared at the Fe sites, and the delocalized π orbitals perpendicular to the plane of the aromatic rings exhibited the lowest ESP distribution (−24.11 ~ −13.03 kcal/mol) (Figure 3C). These results reveal that the strong cation-π interaction promoted the nonuniform distribution

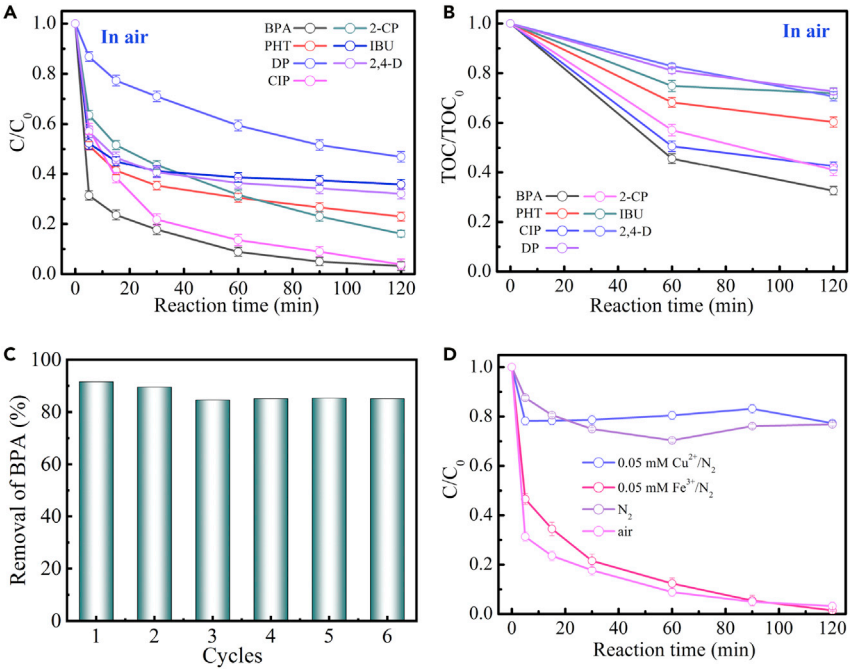

Figure 4. Catalytic performance of Fe^0-Fe_yC_z/Fe_x-GZIF-8-rGO

(A–C) (A) Degradation curves, (B) TOC removal of various organic pollutants, and (C) multiple reaction runs for BPA degradation (reaction time: 120 min per run) in the air-saturated aqueous suspensions of Fe^0-Fe_yC_z/Fe_x-GZIF-8-rGO. (D) BPA degradation in the aqueous suspension of Fe^0-Fe_yC_z/Fe_x-GZIF-8-rGO under different reaction conditions specified in the panel. Reaction conditions: initial pH ~7.0, catalyst concentration 0.6 g L^{-1}, initial organic pollutant concentration 10.0 mg L^{-1}, temperature 35°C. All error bars are calculated from the data of three parallel experiments.

of electrons on the catalyst surface, resulting in the formation of an electron-rich area around the iron species and the electron-poor one around the aromatic rings of GZIF-8 and rGO in Fe^0-Fe_yC_z/Fe_x-GZIF-8-rGO (Lyu et al., 2018a; Kumar et al., 2018). The surface potential energy between both areas might be 663.96/547.38/310.97 kJ/mol.

Fe^0-Fe_yC_z/Fe_x-GZIF-8-rGO performance for pollutants removal

In the air-saturated Fe^0-Fe_yC_z/Fe_x-GZIF-8-rGO aqueous suspension, the pollutants were considerably oxidized and mineralized with increasing the reaction time. Bisphenol A (BPA), ciprofloxacin (CIP), 2-chlorophenol (2-CP), ibuprofen (IBU), 2,4-dichlorophenoxyacetate (2,4-D), diphenhydramine (DP), and phenytoin (PHT) were degraded by approximately 97%, 96.2%, 84%, 64.3%, 68%, 53.1%, and 77.1% within 120 min, respectively (Figure 4A). The total organic carbon (TOC) concentration after 180 min of reaction time was approximately 67.5%, 57.5%, 59.1%, 28.1%, 29.4%, 27.4%, and 39.7%, respectively (Figure 4B). In nano-Fe_3O_4, rGO, and GZIF-8 air-saturated suspension, about 13.4%, 17.9%, and 33.0% of BPA were removed within 120 min, respectively (Figure S4), which come mainly from adsorption of these materials according to BPA desorption phenomena and no intermediate production.

Furthermore, the catalyst activity did not significantly decrease after six consecutive cycles (Figure 4C) for degradation of BPA, and the dissolved iron concentration was 0.13 mg L^{-1} during the reaction, indicating its high stability. Moreover, the structure of Fe^0-Fe_yC_z/Fe_x-GZIF-8-rGO did not change before and after reaction in the XRD pattern and the ^{57}Fe Mössbauer spectra (Figure S5). Furthermore, in the N_2-saturated Fe^0-Fe_yC_z/Fe_x-GZIF-8-rGO suspension with Fe^{3+} addition, the catalyst still exhibited the same activity as that under the air-saturated condition (Figure 4D). In this case, Fe^{2+} was produced in the solution with increasing reaction time (Figure S6), and no significant oxidation was observed without addition of Fe^{3+} or in the presence of Cu^{2+}. Meanwhile, no reduction of Cu^{2+} was observed under the otherwise identical conditions. The results implied that O_2/Fe^{3+} could serve as an electron acceptor for maintaining the degradation of these organic pollutants in the reaction system, indicating activated electrons generation from the surface reaction of these pollutants on Fe^0-Fe_yC_z/Fe_x-GZIF-8-rGO.

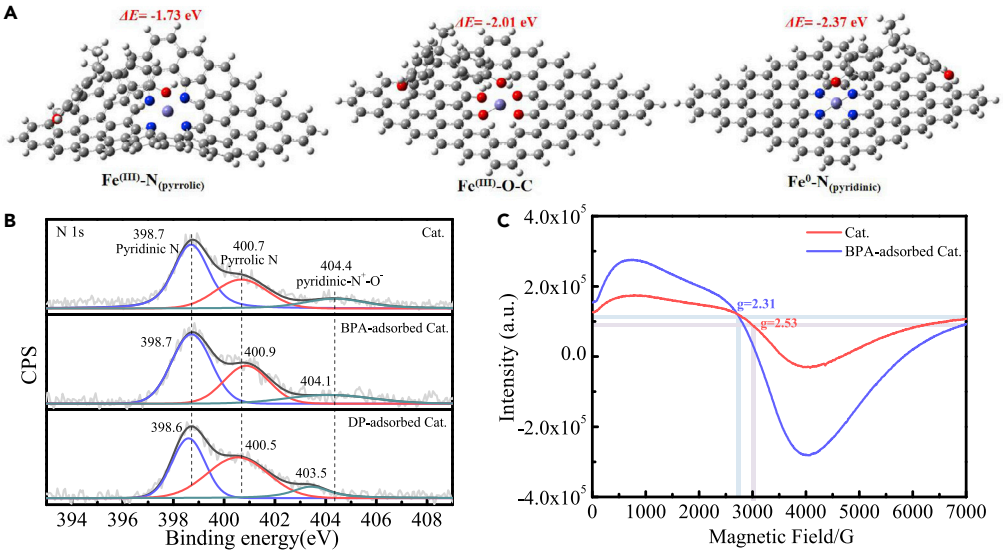

Figure 5. Interaction between Fe^0-Fe_yC_z/Fe_x-GZIF-8-rGO and the organic compounds

(A) Optimal adsorption modes of BPA on different model fragments via DFT calculations.

(B) N 1s XPS spectra of Fe^0-Fe_yC_z/Fe_x-GZIF-8-rGO before and after the adsorptions of BPA and DP in N_2 atmosphere.

(C) EPR spectra of Fe^0-Fe_yC_z/Fe_x-GZIF-8-rGO before and after the adsorption of BPA in N_2 atmosphere. Reaction conditions: (B) initial pH ~7.0, catalyst concentration 0.6 g L^{-1}, initial organic pollutant concentration 10.0 mg L^{-1}, temperature 35°C.

Surface reaction mechanism induced by cation-π interaction

The adsorption isotherms of BPA and DP (Figure S7) were investigated on Fe^0-Fe_yC_z/Fe_x-GZIF-8-rGO with N_2 atmosphere at different temperatures. Langmuir isotherm models is more suitable to fit the experimental data (Table S4), and the adsorption heats (ΔHs) of BPA and DP (Table S5) are 2.852 and 9.793 kJ/mol, respectively (detailed calculation in supplemental information). By DFT calculations, because of the comprehensive effect of the Fe species (Figure 5A), BPA molecules could be stably adsorbed on GZIF-8 and rGO of Fe^0-Fe_yC_z/Fe_x-GZIF-8-rGO by π-π stacking and hydrogen-bond interactions (Yang et al., 2018; Li et al., 2018), with adsorption energies of −1.73, −2.01, and −2.37 eV for $Fe^{(III)}$–$N_{(pyrrolic)}$, $Fe^{(III)}$–O–C, and Fe^0–$N_{(pyridinic)}$ structure models. Moreover, the N 1s XPS spectra including the pyridinic N, pyrrolic N, and pyridinic N^+–O^- exhibited significant shift (Figure 5B) for BPA/DP-adsorbed Fe^0-Fe_yC_z/Fe_x-GZIF-8-rGO, confirming that a strong π-π interaction produced between the aromatic rings of the pollutants and the aromatic rings of GZIF-8/rGO of the catalyst, resulting in the changes of the N 1s bond energies of pyridinic N, pyrrolic N. The electron paramagnetic resonance (EPR) spectroscopy signal of Fe^0-Fe_yC_z/Fe_x-GZIF-8-rGO (Figure 5C) was observed at a g factor of ~2.53, which was attributed to the single electrons in the iron species (Wang et al., 2017), whereas that of BPA-adsorbed Fe^0-Fe_yC_z/Fe_x-GZIF-8-rGO was at a g value of 2.31, and the signal intensity significantly increased, indicating the electrons of the adsorbed group of the BPA molecule were delocalized due to the strong molecular orbital interaction formed between the adsorbed pollutants and GZIF-8/rGO of the catalyst, and migrated around the iron species by the surface potential energy, resulting in the decrease of the bound energy of BPA to the electrons.

O_2 can capture the excess electrons from the surface of metal oxides and transform them into $O_2^{\bullet-}$ (Setvin et al., 2013). By DFT calculations, on all the surface regions of $Fe^{(III)}$–$N_{(pyrrolic)}$, $Fe^{(III)}$–O–C, and Fe^0–$N_{(pyridinic)}$, the O_2 molecules were confined in the micro-areas of the iron species and inclined to stable adsorption at the Fe sites with adsorption energies of −1.08, −2.13, and −2.04 eV (Figure 6A). The EPR signal of BMPO-$O_2^{\bullet-}$ with the hyperfine values of α_N = 14.3 G and α_H = 11.7 G (Buettner, 1987) was observed in Fe^0-Fe_yC_z/Fe_x-GZIF-8-rGO air-saturated suspensions without BPA (Figure 6B), indicating that the single electrons around the iron species could be trapped by O_2. With increasing BPA addition, the $O_2^{\bullet-}$ signal significantly increased by approximately three times from 10 to 50 mg L^{-1}. A similar phenomenon occurred in the Fe^0-Fe_yC_z/Fe_x-GZIF-8-rGO/DP suspension (Figure 6C). This result demonstrated that the electrons from the adsorbed pollutants were captured by O_2 around the Fe species. Moreover, Fe^{3+} in the solution could trap these electrons

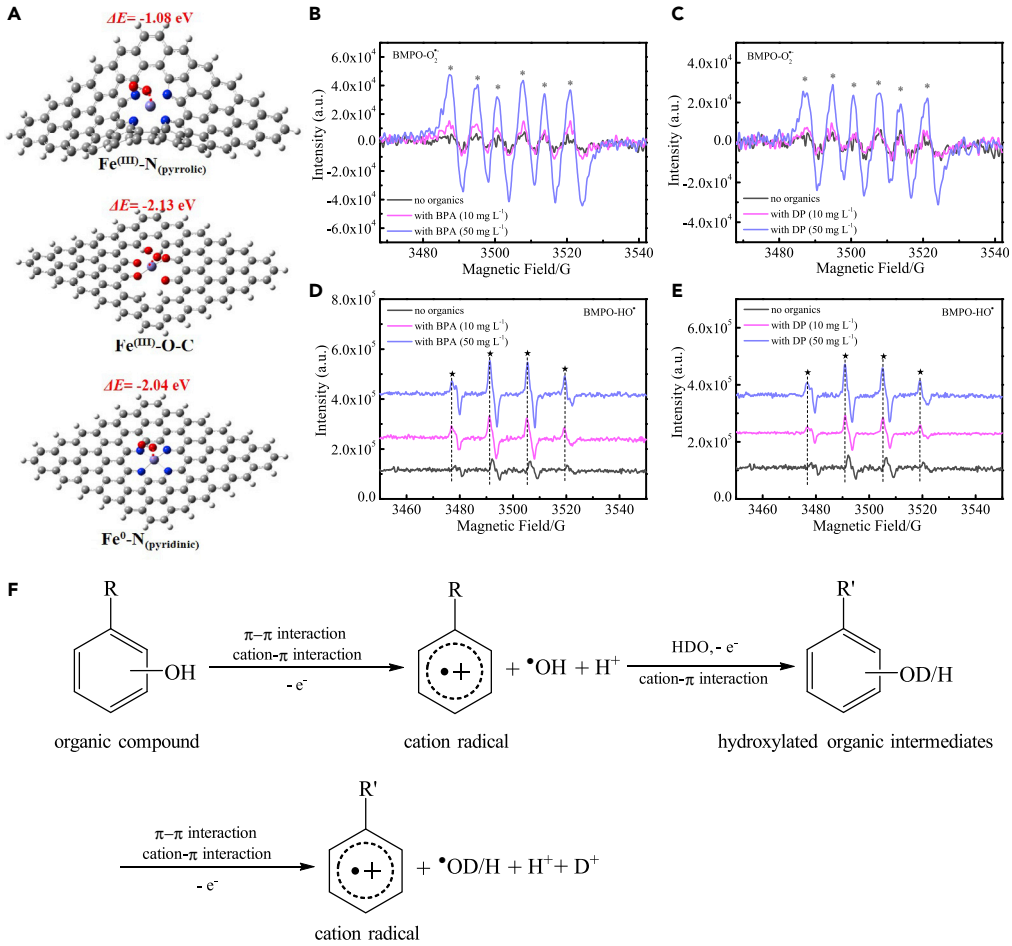

Figure 6. Surface-radical chain reaction onto Fe^0-Fe_yC_z/Fe_x-GZIF-8-rGO

(A) Optimal adsorption modes of O_2 on different model fragments in Fe^0-Fe_yC_z/Fe_x-GZIF-8-rGO by the DFT calculation.

(B–E) BMPO spin-trapping EPR spectra for $O_2^{\bullet-}$ in air-saturated methanol suspensions with/without (B) BPA or (C) DP, and for $^{\bullet}OH$ in the air-saturated D_2O suspensions with/without (D) BPA or (E) DP.

(F) Schematic illustration of the radical chain reaction between organic compounds and the H_2O molecules.

to Fe^{2+} (Figure S6), whereas Cu^{2+} was unable to, indicating that the electrons were bounded by more than the redox potential of Cu^{2+} to Cu^{+} (0.159 V) around the Fe species. Meanwhile, the 4-fold characteristic peak of BMPO-$^{\bullet}OH$ adducts ($\alpha_N = \alpha_H = 14.9$ G) (Buettner, 1987) with an intensity ratio of 1:2:2:1 was detected in Fe^0-Fe_yC_z/Fe_x-GZIF-8-rGO in an aqueous suspension that was equilibrated with air or a solution containing Fe^{3+} that was equilibrated with N_2 (Figures S8A and S8B), and the EPR signal was increased with increasing reaction time. The results demonstrated that the surface-adsorbed H_2O could donate an electron to O_2 or Fe^{3+}, forming $^{\bullet}OH$. For BPA/DP that was equilibrated with air (Figures 6D and 6E) or a solution containing Fe^{3+} that was equilibrated with N_2 in deuterium oxide (D_2O) suspensions (Figures S8C and S8D), the BMPO-$^{\bullet}OH$ signals enhanced greatly with increasing concentrations of BPA/DP. Particularly, the positions of the four peaks shifted significantly compared with those without pollutants, indicating that both H and –OH of BPA/DP were converted to H and $^{\bullet}OH$ in solution by surface reaction, and some intermediates were hydrolyzed into hydroxylated products, according to the exchange of H^+ and D_2O.

Based on both the by-products of pollutants in the solution and on the catalyst surface for 60 and 120 min (Figures S9 and S10; Tables S6 and S7), the positions at the phenolic group and 2-propyl connecting both benzene ring in BPA were broken, producing benzoic acid, benzene, methylmalonic acid, et al. Subsequently, benzene was reduced to cyclohexene; the benzene ring of part benzoic acid was cleaved to form methylmalonic acid, and then most of intermediates were converted into CO_2, H_2O (Figure S11). Similarly, for CIP, the branches of benzene ring were broken. The next hydrogenation or hydroxylation

produced benzene, 3,4-dihydroxyphenylglycol, 3-cyclohexene-1-carboxaldehyde, and benzoic acid. Finally, some organic acid and alcohol formed with CO_2, H_2O, F^-, and NO_3^- (Figures S12 and S13).

According to DFT calculations, for BPA (Figure S14), both phenolic groups and the carbon atoms of the aromatic ring belong to the highest occupied molecular orbital (HOMO), whereas the other moieties of BPA belong to the lowest unoccupied molecular orbital (LUMO). Similarly, for the structure of CIP, the F group, N-containing organic group, and carbonyl group connecting to benzene ring were in the HOMO, whereas the other moieties were in LUMO.

$$D^+ + OD^- + H^+ \rightleftharpoons D^+ + HDO \quad \text{(Equation 1)}$$

Based on the above experimental data, the main surface reaction process was proposed (Figure 6F). By the surface potential energy (663.96 or 547.38 or 310.97 kJ/mol), on the adsorbed organic pollutants, these electrons on HOMO tended to delocalize and store around the Fe species. Thereafter, these electrons were trapped by O_2 or Fe^{3+} to form $O_2^{\bullet-}$ or Fe^{2+} in suspension, leading to the adsorbed hydroxyl and aromatic ring groups were converted into H^+ and $^{\bullet}OH$, organic cation radicals. Subsequently, the H^+ exchanged with D^+ of D_2O to HDO (Equation 1), and the organic cation radicals underwent hydrogenation or hydroxylation to form hydroxylated organic intermediates (R′-OD/H). Then, the same surface reaction process recurred over and over, which converted water molecules into $^{\bullet}OH$, which is responsible for the destruction and mineralization of organics in solution. Accordingly, our findings could be applied to the development of new catalytic processes in industries and environmental protection.

Real wastewater treatment with Fe^0-Fe_yC_z/Fe_x-GZIF-8-rGO

Three kinds of wastewater were collected from the effluent after biological treatment of dyeing, kitchen, and urban wastewaters in Guangdong Province, China, and the initial chemical oxygen demand (COD) was 87.0, 359.9, and 20.8 mg/L, respectively. Then, they were treated over Fe^0-Fe_yC_z/Fe_x-GZIF-8-rGO air-saturated suspension. About 23.5%, 73.9%, and 60.7% of COD was removed for dyeing, kitchen, and urban wastewaters within 120 min (Figure S15). Since three-dimensional excitation and emission matrix (3D-EEM) fluorescence spectra could reflect the degree of organic pollution in water (Wu et al., 2016; Tang et al., 2018), they were measured with the degradation of COD (Figures S16–S18). The fluorescence intensity of these peaks at Ex/Em of 229–239/353–375 nm (peak A) for the aromatic proteins, 281–289/350-359 nm (peak B) for protein-like compounds, and 244–250/415-465 nm (peak C) fulvic-like compounds, and the other peaks at 310/465 nm (peak D), 360/463 nm (peak E), and 322–332/405–417 nm (peak F) for humic-like compounds (Chen et al., 2003) all significantly gradually weakened with increasing reaction time for the three wastewaters. The results indicated that organic pollutants in these real wastewaters were efficiently destructed over Fe^0-Fe_yC_z/Fe_x-GZIF-8-rGO by the surface cleavage and the oxidation of $^{\bullet}OH$. The results demonstrated that Fe^0-Fe_yC_z/Fe_x-GZIF-8-rGO is a promising catalyst for practical wastewater remediation with little energy input.

Limitations of the study

The current study reports an ingenious method for the fabrication of Fe^0-Fe_yC_z/Fe_x-GZIF-8-rGO composite with the properties of strong cation-π interaction. However, at the current stage, the synthetic process is complicated and the yield of product is relatively low. Thus, further optimizations are required to lower the cost and improve catalytic efficiency for practical applications. In addition, the exact bound energy of the surface to the delocalized electron belonging to the adsorbed group of organic pollutants could not be accurately determined in the Fe^0-Fe_yC_z/Fe_x-GZIF-8-rGO suspension owing to the lack of characterization method at present.

STAR★METHODS

Detailed methods are provided in the online version of this paper and include the following:

- KEY RESOURCES TABLE
- RESOURCE AVAILABILITY
  - Lead contact
  - Materials availability
  - Data and code availability
- METHOD DETAILS
  - Synthesis of GO
  - Synthesis of nano-Fe_3O_4

SUPPLEMENTAL INFORMATION

Supplemental information can be found online at https://doi.org/10.1016/j.isci.2021.102874.

ACKNOWLEDGMENTS

This work was supported by the National Natural Science Foundation of China (51838005), the introduced innovative R&D team project under the "The Pearl River Talent Recruitment Program" of Guangdong Province (2019ZT08L387), and the National Key Research and Development Plan (2016YFA0203200). The authors appreciate the support from the 1W1B-XAFS beamline of the Beijing Synchrotron Radiation Facility (BSRF, China). Also, the authors appreciate the support from the Brook Byers Institute for Sustainable Systems, Hightower Chair and Georgia Research Alliance at the Georgia Institute of Technology. The views and ideas expressed herein are solely those of the authors and do not represent the ideas of the funding agencies in any form.

AUTHOR CONTRIBUTIONS

C. H. supervised the project and designed the experiments. Y. W. and L. L. contributed equally to this work. F. L., D. W., L. Z., Y. G., and T. L. assisted in characterization of materials. H.-Q. Y. and J. C. C. discussed the experimental data with us (C. H., Y. W. and L. L.).

DECLARATION OF INTERESTS

A China provisional patent application (no. 202010562502.9) for this work was filed on 18 June, 2020 by C. H., Y. W., and L. L. at Guangzhou University. The other authors declare no competing interests.

Received: May 13, 2021
Revised: June 27, 2021
Accepted: July 14, 2021
Published: August 20, 2021

REFERENCES

Abednatanzi, S., Derakhshandeh, P.G., Leus, K., Vrielinck, H., Callens, F., Schmidt, J., Savateev, A., and VanDer Voort, P.((2020). Metal-free activation of molecular oxygen by covalent triazine frameworks for selective aerobic oxidation. Sci. Adv. *6*, eaaz2310.

Algara-Siller, G., Lehtinen, O., Wang, F.C., Nair, R.R., Kaiser, U., Wu, H.A., Geim, A.K., and Grigorieva, I.V. (2015). Square ice in graphene nanocapillaries. Nature *519*, 443–445.

Adewuyi, Y.G. (2005). Sonochemistry in environmental remediation. 1. Combinative and hybrid sonophotochemical oxidation processes for the treatment of pollutants in water. Environ. Sci. Technol. *39*, 8557–8570.

Bing, J., Hu, C., Nie, Y., Yang, M., and Qu, J. (2015). Mechanism of catalytic ozonation in Fe_2O_3/Al_2O_3@SBA-15 aqueous suspension for destruction of ibuprofen. Environ. Sci. Technol. *49*, 1690–1697.

Buettner, G.R. (1987). Spin trapping: ESR parameters of spin adducts. Free Radic. Bio. Med. *3*, 259–303.

Bullock, A. (2003). Water for People, Water for Life—The United Nations World Water Development Report (World Water Assessment Programme press).

Chen, W., Westerhoff, P., Leenheer, J.A., and Booksh, K. (2003). Fluorescence excitation-emission matrix regional integration to quantify spectra for dissolved organic matter. Environ. Sci. Technol. *37*, 5701–5710.

Chen, Y., Ji, S., Zhao, S., Chen, W., Dong, J., Cheong, W.C., Shen, R., Wen, X., Zheng, L., Rykov, A.I., et al. (2018). Enhanced oxygen reduction with single-atomic-site iron catalysts for a zinc-air battery and hydrogenair fuel cell. Nat. Commun. *9*, 5422.

Deakyne, C.A., and Meot-Ner, M. (1985). Unconventional hydrogen bonds. 2. NH^+–π complexes of onium ions with olefins and benzene derivatives. J. Am. Chem. Soc. *107*, 474–479.

Dougherty, D.A. (1996). Cation-π interactions in chemistry and biology: a new view of benzene, phe, tyr, and trp. Science *271*, 163.

Gebbie, M.A., Wei, W., Schrader, A.M., Cristiani, T.R., Dobbs, H.A., Idso, M., Chmelka, B.F., Waite, J.H., and Israelachvili, J.N. (2017). Tuning underwater adhesion with cation–π interactions. Nat. Chem. *9*, 473–479.

Georgakilas, V., Otyepka, M., Bourlinos, A.B., Chandra, V., Kim, N., Christian Kemp, K., Hobza, P., Zboril, R., and Kim, K.S. (2012).

Functionalization of graphene: covalent and non-covalent approaches, derivatives and applications. Chem. Rev. *112*, 6156–6214.

Gu, J., Hsu, C.S., Bai, L., Chen, H.M., and Hu, X. (2019). Atomically dispersed Fe^{3+} sites catalyze efficient CO_2 electroreduction to CO. Science *364*, 1091–1094.

Han, M., Lyu, L., Huang, Y., Liang, J., Xue, M., Wu, T., Li, J., Chen, M., and Hu, C. (2019). In situ generation and efficient activation of H_2O_2 for pollutant degradation over $CoMoS_2$ nanosphere-embedded rGO nanosheets and its interfacial reaction mechanism. J. Colloid Interface Sci. *543*, 214–224.

Hummers, W., and Offeman, R. (1958). Preparation of graphitic oxide. J. Am. Chem. Soc. *80*, 1339.

Jiang, N., Lyu, L., Yu, G., Zhang, L., and Hu, C. (2018). A dual-reaction-center Fenton-like process on –C≡N–Cu linkage between copper oxides and defect-containing g-C_3N_4 for efficient removal of organic pollutants. J. Mater. Chem. A *6*, 17819–17828.

Jin, H., Tian, X., Nie, Y., Zhou, Z., Yang, C., Li, Y., and Lu, L. (2017). Oxygen vacancy promoted heterogeneous Fenton-like degradation of ofloxacin at pH 3.2−9.0 by Cu substituted magnetic Fe_3O_4@FeOOH nanocomposite. Environ. Sci. Technol. *51*, 12699–12706.

Kumar, K., Woo, S.M., Siu, T., Cortopassi, W.A., Duarte, F., and Paton, R.S. (2018). Cation-π interactions in protein-ligand binding: theory and data-mining reveal different roles for lysine and arginine. Chem. Sci. *9*, 2655–2665.

Lagutschenkov, A., Sinha, R.K., Maitre, P., and Dopfer, O. (2010). Structure and infrared spectrum of the Ag^+-Phenol ionic complex. J. Phys. Chem. A *114*, 11053–11059.

Lee, J., Gunten, U., and Kim, J.H. (2020). Persulfate-based advanced oxidation: critical assessment of opportunities and roadblocks. Environ. Sci. Technol. *54*, 3064–3081.

Liang, B., Sun, T., Ma, J., Duan, H., Li, L., Yang, X., Zhang, Y., Su, X., Huang, Y., and Zhang, T. (2019). Mn decorated Na/Fe catalysts for CO_2 hydrogenation to light olefins. Catal. Sci. Technol. *9*, 456–464.

Liu, G., Li, X., Ganesan, P., and Popov, B.N. (2009). Development of non-precious metal oxygen-reduction catalysts for PEM fuel cells based on N-doped ordered porous carbon. Appl. Catal. B: Environ. *93*, 156–165.

Li, J., Chen, C., Zhang, R., and Wang, X. (2015a). Nanoscale zero-valent iron particles supported on reduced graphene oxides by using a plasma technique and their application for removal of heavy-metal ions. Chem. Asian J. *10*, 1410–1417.

Li, W., Yu, H., and Rittmann, B.E. (2015b). Reuse water pollutants. Nature *528*, 29–31.

Li, X., Li, X.M., Jiang, Y., Liu, Z., Cui, Y., Fung, K.Y., van der Beelen, S.H.E., Tian, G., Wan, L., Shi, X., et al. (2018). Structure-guided development of YEATS domain inhibitors by targeting π-π-π stacking. Nat. Chem. Biol. *14*, 1140–1149.

Li, W., Zhang, Y., Su, P., Xu, Z., Zhang, G., Shen, C., and Meng, Q. (2016). Metal-organic framework channelled graphene composite membranes for H_2/CO_2 separation. J. Mater. Chem. A *4*, 18747–18752.

Luo, G., Jiang, X., Li, M., Shen, Q., Zhang, L., and Yu, H. (2013). Facile fabrication and enhanced photocatalytic performance of Ag/AgCl/rGO heterostructure photocatalyst. ACS Appl. Mater. Interfaces *5*, 2161–2168.

Lyu, L., Yan, D., Yu, G., Cao, W., and Hu, C. (2018a). Efficient destruction of pollutants in water by a dual-reaction center Fenton-like process over carbon nitride compounds complexed Cu(II)-$CuAlO_2$. Environ. Sci. Technol. *52*, 4294–4304.

Lyu, L., Yu, G., Zhang, L., Hu, C., and Sun, Y. (2018b). 4-Phenoxyphenol-Functionalized reduced graphene oxide nanosheets: a metal-free fenton-like catalyst for pollutant destruction. Environ. Sci. Technol. *52*, 747–756.

Lyu, L., Zhang, L., He, G., He, H., and Hu, C. (2017). Selective H_2O_2 conversion to hydroxyl radicals in the electron-rich area of hydroxylated C-g-C_3N_4/CuCo–Al_2O_3. J. Mater. Chem. A *5*, 7153.

Ma, J.C., and Dougherty, D.A. (1997). The cation–π interaction. Chem. Rev. *97*, 1303–1324.

Meng, F., Li, J., Cushing, S.K., Bright, J., Zhi, M., Rowley, J.D., Hong, Z., Manivannan, A., Bristow, A.D., and Wu, N. (2013). Photocatalytic water oxidation by hematite/reduced graphene oxide composites. ACS Catal. *3*, 746–751.

Moon, I.K., Lee, J., Ruoff, R.S., and Lee, H. (2010). Reduced graphene oxide by chemical graphitization. Nat. Commun. *1*, 73.

Salonen, L.M., Ellermann, M., and Diederich, F. (2011). Aromatic rings in chemical and biological recognition energetics and structures. Angew. Chem. Int. Ed. *50*, 4808–4842.

Schwarzenbach, R.P., Escher, B.I., Fenner, K., Hofstetter, T.B., Johnson, A., Gunten, U., and Wehrli, B. (2006). The challenge of micropollutants in aquatic systems. Science *313*, 1072–1077.

Setvin, M., Aschauer, U., Scheiber, P., Li, Y.F., Hou, W., Schmid, M., Selloni, A., and Diebold, U. (2013). Reaction of O_2 with subsurface oxygen vacancies on TiO_2 anatase (101). Science *341*, 988–991.

Tang, J., and Wang, J. (2018). Metal organic framework with coordinatively unsaturated sites as efficient Fenton-like catalyst for enhanced degradation of sulfamethazine. Environ. Sci. Technol. *52*, 5367–5377.

Tang, X., Liu, Y., Wang, J., Zeng, G., Deng, Y., Dong, H., Feng, H., Wang, J., and Peng, B. (2018). Enhanced activation process of persulfate by mesoporous carbon for degradation of aqueous organic pollutants: electron transfer mechanism. Appl. Catal. B Environ. *231*, 1–10.

Teixido, M., Pignatello, J.J., Beltran, J.L., Granados, M., and Peccia, J. (2011). Speciation of the ionizable antibiotic sulfamethazine on black carbon (biochar). Environ. Sci. Technol. *45*, 10020–10027.

van Genuchten, C.M., Behrends, T., Kraal, P., Stipp, S.L.S., and Dideriksen, K. (2018). Controls on the formation of Fe(II,III) (hydr)oxides by Fe(0) electrolysis. Electrochim. Acta *286*, 324–338.

Wang, J., Chen, Z., and Chen, B. (2014). Adsorption of polycyclic aromatic hydrocarbons by graphene and graphene oxide nanosheets. Environ. Sci. Technol. *48*, 4817–4825.

Wang, Q., Lei, Y., Chen, Z., Wu, N., Wang, Y., Wang, B., and Wang, Y. (2018). Fe/Fe_3C@C nanoparticles encapsulated in N-doped graphene–CNTs framework as an efficient bifunctional oxygen electrocatalyst for robust rechargeable Zn–air batteries. J. Mater. Chem. A *6*, 516–526.

Wang, T., Qi, L., Lu, H., and Ji, M. (2017). Flower-like Al_2O_3-supported iron oxides as an efficient catalyst for oxidative dehydrogenation of ethlybenzene with CO_2. J. Co_2. Util. *17*, 162–169.

Wu, J., Ma, L., Chen, Y., Cheng, Y., Liu, Y., and Zha, X. (2016). Catalytic ozonation of organic pollutants from bio-treated dyeing and finishing wastewater using recycled waste iron shavings as a catalyst: removal and pathways. Water Res. *92*, 140–148.

Wu, S., Cajthaml, T., Semerád, J., Filipová, A., Klementová, M., Skála, R., Vítková, M., Michálková, Z., Teodoro, M., Wu, Z., et al. (2019). Nano zero-valent iron aging interacts with the soil microbial community: a microcosm study. Environ. Sci. Nano *6*, 1189–1206.

Yamada, S. (2018). Cation-π interactions in organic synthesis. Chem. Rev. *118*, 11353–11432.

Yang, J., Zhen, X., Wang, B., Gao, X., Ren, Z., Wang, J., Xie, Y., Li, J., Peng, Q., Pu, K., et al. (2018). The influence of the molecular packing on the room temperature phosphorescence of purely organic luminogens. Nat. Commun. *9*, 840.

Yang, Q., Chen, Y., Duan, X., Zhou, S., Niu, Y., Sun, H., Zhi, L., and Wang, S. (2020). Unzipping carbon nanotubes to nanoribbons for revealing the mechanism of nonradical oxidation by carbocatalysis. Appl. Catal. B: Environ. *276*, 119146.

Zangmeister, C. (2010). Preparation and evaluation of graphite oxide reduced at 220 oC. Chem. Mater. *22*, 5625–5629.

Zhang, H., Fan, X., Quan, X., Chen, S., and Yu, H. (2011). Graphene sheets grafted Ag@AgCl hybrid with enhanced plasmonic photocatalytic activity under visible light. Environ. Sci. Technol. *45*, 5731–5736.

Zitolo, A., Goellner, V., Armel, V., Sougrati, M.T., Mineva, T., Stievano, L., Fonda, E., and Jaouen, F. (2015). Identification of catalytic sites for oxygen reduction in iron- and nitrogen-doped graphene materials. Nat. Mater. *14*, 937–942.

STAR★METHODS

KEY RESOURCES TABLE

REAGENT or RESOURCE	SOURCE	IDENTIFIER
Chemicals, peptides, and recombinant proteins		
Zinc nitrate hexahydrate	Guangzhou Chemical	CAS: 10196-18-6
Polyvinylpyrrolidone	Damao Chemical	CAS: 9003-39-8
Iron(III) chloride hexahydrate	Titan	CAS: 10025-77-1
L (+)-Ascorbic acid	Titan	CAS: 50-81-7
sodium bicarbonate	Titan	CAS: 144-55-8
5-tert-butoxycarbonyl-5-methyl-1-pyrroline-N-oxide (BMPO)	Dojindo	CAS: 387334-31-8
bisphenol A	Adamas	CAS: 80-05-7
2-chlorophenol	Adamas	CAS: 95-57-8
Phenytoin	Adamas	CAS: 57-41-0
2, 4-dichlorophenoxyacetate	Adamas	CAS: 94-75-7
Ibuprofen	Adamas	CAS: 15687-27-1
Diphenhydramine	Shanghai TCI	CAS: 147-24-0
Ciprofloxacin	Shanghai TCI	CAS: 85721-33-1
deuterium oxide	Adamas	CAS: 7789-20-0
Software and algorithms		
Origin 8.1	OriginLab	https://www.originlab.com/
Excel	Microsoft	N/A

RESOURCE AVAILABILITY

Lead contact

Further information and requests for resources and reagents should be directed to and will be fulfilled by the lead contact, Chun Hu (huchun@gzhu.edu.cn).

Materials availability

This study did not generate new unique reagents.

Data and code availability

- Data reported in this paper will be shared by the lead contact upon request.
- This paper does not report original code.
- Any additional information required to reanalyze the data reported in this paper is available from the lead contact upon request.

METHOD DETAILS

Synthesis of GO

Graphene oxide (GO) was prepared by a modified hummers method through the oxidation of graphite powde (Hummers and Offeman, 1958; Zangmeister, 2010). Typically, the solid GO sample was prepared by the same procedure as that of our previous work (2018b). 5.0 g of graphite was placed into 115 mL of cold concentrated H_2SO_4 solution in an ice bath below 0°C. Then, 25.0 g of $NaNO_3$ was added to the solution, which was magnetically stirred for 30 min. $KMnO_4$ (15.0 g) was then gradually added to the above mixture under stirring, and the temperature of the mixture was kept below 0°C for 3.0 h. The mixture was then transferred to a water bath and magnetically stirred at 38°C for 30 min. After that, 250 mL deionized water was slowly added to the mixture under stirring, and the temperature of the mixture was raised to 95°C. After reacting for 1.0 h, 50 mL H_2O_2 (30 wt%) was added into the above solution to quench the

reaction and produce a golden-brown solution. The sample was subsequently washed with diluted HCl solution and deionized water dozens of times via centrifugation until the pH of the washing solution was ~6. Finally, the product was dried at 70°C to obtain the solid GO sample.

Synthesis of nano-Fe_3O_4

Nano-Fe_3O_4 was prepared by a hydrothermal process. Generally, 0.176 g of L (+)-ascorbic acid was dissolved in 20 mL of deionized water. Following this, 1.62 g of $FeCl_3 \cdot 6H_2O$ and 1.52 g of $NaHCO_3$ were dissolved in 60 mL of deionized water and stirred for 30 min at room temperature. Both solutions were placed in a Teflon-lined steel autoclave and heated for 8 h at 150°C. After cooling naturally, the obtained nano-Fe_3O_4 was washed with and dispersed in methanol for the subsequent experiments.

Synthesis of Fe^0-Fe_yC_z/Fe_x-GZIF-8-rGO

The Fe^0-Fe_yC_z/Fe_x-GZIF-8-rGO catalyst was prepared using a calcination method. First, 3 g of 2-methylimidazole and 0.25 g of the as-prepared nanoFe_3O_4, dispersed in 10 mL of methanol, were added to 60 mL of methanol to obtain suspension A. Thereafter, 0.8 g of $Zn(NO_3)_2 \cdot 6H_2O$, 0.9 g of polyvinylpyrrolidone, and 0.06 g of GO were mixed in 60 mL of methanol to obtain solution B. After they were treated with ultrasound for 30 min, B was added to A and stirred for 6 h, followed by aging for 48 h at room temperature. The resulting sample was washed with ethanol, dried overnight in an oven at 60°C, and calcinated for 2 h at 700°C in an N_2 atmosphere. Finally, Fe^0-Fe_yC_z/Fe_x-GZIF-8-rGO was obtained as the product after cooling and washing with deionized water. As a reference, both GZIF-8-rGO and GZIF-8 were prepared using identified conditions without the additions of nano-Fe_3O_4 or GO and nano-Fe_3O_4.

Characterizations

The XRD patterns of all the samples were recorded in the range of 5°–90° (2θ) on a Scintag-XDS-2000 diffractometer with Cu Kα radiation (λ = 1.540598 Å) operating at 40 kV and 40 mA. The Raman spectra were recorded on a LabRAM HR Evolution (HORIBA, France) equipped with a CCD detector utilizing a laser source at an excitation line of 532 nm. The XPS data were recorded on an AXIS-Ultra instrument utilizing monochromatic Al Kα radiation (225 W, 15 mA, 15 kV) and low-energy electron flooding for the charge compensation. The binding energies were calibrated with the C 1s hydrocarbon peak at 284.8 eV. The EPR spectra of the solid samples were obtained on a Bruker A300-10/12 electron paramagnetic resonance spectrometer. The Fe K-edge EXAFS spectra were measured at room temperature in the transmission mode at the 1W1B beamline of the Beijing Synchrotron Radiation Facility (BSRF, China). The room-temperature ^{57}Fe Mössbauer spectra were measured on a Mössbauer spectrometer (Wissel, Germany) with a radioactive source of 25 mCi ^{57}Co (Pd).

General catalytic procedures

All the experiments were performed at a concentration of 0.6 g L^{-1} for the catalyst and an initial concentration of 10 mg L^{-1} for the organic pollutants, unless otherwise specified. In the typical experiment, 0.03 g of the Fe^0-Fe_yC_z/Fe_x-GZIF-8-rGO powders were added to a 50 mL solution containing 10 mg L^{-1} organic pollutants and magnetically stirred throughout the reaction time. At given intervals, 1 mL aliquots were collected, centrifuged, and filtered through a Millipore filter (pore size, 0.22 μm) to remove the particulates of the catalyst for analysis. The concentration of the organic pollutant was analyzed by a 1200 series HPLC (Agilent, USA). The total organic carbon of the solution was analyzed with a TOC-L CPH CN200 (Shimadzu, Japan) TOC analyzer. GC–MS analysis and the preparation of the samples are described below. The catalyst was recycled by simple filtration without any treatment for each experiment cycle. Furthermore, to study the durability of Fe^0-Fe_yC_z/Fe_x-GZIF-8-rGO, BPA was degraded for 120 min in the Fe^0-Fe_yC_z/Fe_x-GZIF-8-rGO air-saturated aqueous dispersion.

GC-MS analysis

The samples for gas chromatography-mass spectroscopy (GC-MS) analyses were prepared as follows: the suspensions were filtered at different reaction times to obtain a solid catalyst and solution. Thereafter, the solution was evaporated in a vacuum freeze-drying oven. Subsequently, the residues were dissolved with 2 mL of dichloromethane, followed by trimethylsilylated with 0.2 mL N,O-bis(trimethylsilyl)trifluoroacetamide (BTFA, TCI) at 60 °C for 30 min. Finally, the precipitate was separated by centrifugation before the chromatographic analysis. GC-MS analysis was performed on an Agilent 6890GC/5973MSD GC mass

spectrometer equipped with a capillary column (DB-5 MS). The chromatographic conditions were as follows: the initial column temperature was held for 2 min at 333 K before it was ramped to 553 K at 6 K/min.

DFT CALCULATIONS

The models of different fragments were developed with a GaussView. The dangling bonds of the edge atoms were terminated by hydrogen atoms to obtain a neutral cluster. All the calculations were performed on the Gaussian 09 program. The B3lyp-D3 method was employed for the optimization of the models. The ESP distributions were constructed from the cube files of the DFT calculations employing the VMD program. The adsorption energy (ΔE) was estimated via the following formula: ΔE (ads) = E (surface + mol) − E(surface) − E (mol) + E (BSSE)

$$\Delta E\ (ads) = E\ (surface + mol) - E(surface) - E\ (mol) + E\ (BSSE),$$

where E (surface + mol) is the total energy of the Fe^0-Fe_yC_z/Fe_x-GZIF-8-rGO surface-adsorbed bisphenol A (BPA) and oxygen (O_2) molecules, E(surface) is the total energy of the Fe^0-Fe_yC_z/Fe_x-GZIF-8-rGO surface, E (mol) is the total energy of the BPA and the oxygen (O_2) molecules, and E(BSSE) is the basis set superposition error of the LCAO method.

Owing to the size and edge effects, the properties that were estimated with the finite-size model may vary from those of the real system to some extent. However, it can be expected that the results obtained with the current model would be qualitatively reliable in predicting the local chemical properties.

ISOTHERMAL ADSORPTION EXPERIMENT

All the adsorption isotherms for BPA and DP were obtained in 100 mL of 0.6 g L^{-1} Fe^0-Fe_yC_z/Fe_x-GZIF-8-rGO N_2-saturated suspensions at 25, 35, and 45 ± 2 °C. The suspensions were equilibrated for 24 h in a temperature-controlled shaker, and the obtained aliquots were analyzed with a 1200 series HPLC (Agilent, USA).

These data (Table S4) from the adsorption isotherms were obtained by fitting the Langmuir and Freundlich isotherm models:

$$\frac{C_e}{Q_e} = \frac{1}{Q_{maxb}} + \frac{C_e}{Q_{max}}\ (\text{Langmuir model})$$

$$\log Q_e = \log K_F + \frac{1}{n}\log C_e (\text{Freundlich model}),$$

where C_e is the equilibrium concentration (mg L^{-1}), Q_e is the amount adsorbed at equilibrium (mg/g), Q_{max} is the adsorption capacity for the Langmuir isotherms, and '*b*' is the equilibrium constant. Furthermore, 'n' indicates the degree of favorability of adsorption (as 1/n decreases the isotherm become more favorable and K_F is the isotherm capacity constant.

The thermodynamic parameters (Table S5) were obtained from the following equations:

$$b = \frac{Q_e}{C_e}$$

$$\Delta G = -RT\ \ln b$$

$$\log b = \frac{\Delta S}{2.303R} - \frac{\Delta H}{2.303TR},$$

where C_e is the equilibrium concentration of the solution (mgL^{-1}), Q_e is the equilibrium concentration on the adsorbent (mg L^{-1}), and 'b' is the equilibrium constant. The values of ΔH and ΔS can be obtained from the slope and intercept of the plot of ln*b* vs. 1/*T*.

Detection of $^{\cdot}OH$ and $O_2^{\cdot-}$ EPR signals

The BMPO-trapped EPR signals were detected in Fe^0-Fe_yC_z/Fe_x-GZIF-8-rGO methanol/aqueous dispersions with/without the organic pollutants with a Bruker A300-10/12 EPR spectrometer at room temperature in air or N_2 atmosphere. Typically, 0.01 g of the prepared powder sample was added to 1 mL of H_2O/D_2O (for the detection of $^{\cdot}OH$) or methanol (for the detection of $O_2^{\cdot-}$). Thereafter, 20 μL of BMPO (250 mM) was

added, and the solution was left to stand for a specified contact time. Following this, the solution was sucked into a capillary tube for EPR detection.

Determination of Fe^{2+} concentration

To investigate the interface reaction mechanism, the production of Fe^{2+} was examined in the N_2-saturated Fe^0-Fe_yC_z/Fe_x-GZIF-8-rGO aqueous dispersion containing BPA (10 mg L^{-1}) with Fe^{3+} (0.05 mM) in the solution. The phenanthroline spectrophotometric method described by Bing et al. (Bing et al., 2015) was employed to detect Fe^{2+} in the solution by recording the absorbance at 510 nm with an ultraviolet–visible (UV-vis) spectrophotometer (UH4150, HITACHI).

Determination of chemical oxygen demand

10 mL water sample was added in to a conical flask, and then mixed with a certain volume of mercury sulfate and potassium dichromate solutions. After adding a few glass beads and 15 mL silver nitrate-sulfuric acid solution, the mixture was digested for 2 h in a HCA-112 COD digester. When cooled down to room temperature, 45 mL deionized water was added and the resulted mixed solution was titrated using ammonium ferrous sulfate solution.

3D-EEM fluorescence measurements

The 3D-EEM fluorescence spectra of various samples were obtained on an F-7000 spectrometer (HITACHI) with a xenon excitation source, and slits were set to 5 nm for both excitation and emission. The excitation wavelengths were incremented from 200 to 420 nm in 5-nm steps; for each excitation wavelength, the emission was detected from 280 to 550 nm in 3-nm steps.